05,12

Phase transitions and phase transformations in the phase separation nanoregions in $ErMn_2O_5$ multiferroics

© B.Kh. Khannanov, V.A. Sanina¶, E.I. Golovenchits, S.G. Lushnikov

Ioffe Institute,
St. Petersburg, Russia

¶ E-mail: sanina@mail.ioffe.ru

Received June 24, 2021
Revised June 24, 2021
Accepted June 27, 2021

The effect of the rare-earth ion Er^{3+}, which has a large orbital contribution to the magnetic moment, were studied to phase transitions and phase transformations of 2D nanoregions of phase separation in the $ErMn_2O_5$ multiferroic. These nanoregions are the semiconductor heterostructures (superlattices) and are formed due to self-organization processes in the $ErMn_2O_5$ matrix. Significant effect of Er^{3+} ions, the moments of which are rigidly oriented along the c axis of the crystal, on the magnetic dynamics, heat capacity and multiferroic properties of layers superlattises was found at a wide temperature range 5−300 K in $ErMn_2O_5$ multiferroics.

Keywords: multiferroic, 2D phase separation nanoregions, semiconductor-heterostructures, superlattices, phase transitions, phase transformations.

DOI: 10.21883/PSS.2022.13.52313.155

1. Introduction

RMn_2O_5 (R are rare-earth ions, Bi) crystals are type-II multiferroics with ferroelectric ordering induced in them below the Curie temperature ($T_C \approx 30-35$ K) by magnetic ordering with Néel temperature $T_N \approx 35-40$ K [1,2]. At room temperature, they are characterized by centrosymmetric space group $Pbam$ [3]. Since the temperatures of magnetic and ferroelectric ordering are close, these multiferroics feature a strong magnetoelectric effect.

The specific feature of RMn_2O_5 is the presence of equal numbers of Mn^{3+} ions (containing three t_{2g} electrons and one e_g electron in the $3d$ shell) and Mn^{4+} ions (with three t_{2g} electrons in the $3d$ shell). This provides the conditions needed for dielectric charge ordering. Mn^{4+} ions have an octahedral oxygen environment and are positioned in layers with $z = 0.25c$ and $(1-z) = 0.75c$. Coupled chains of octahedra with Mn^{4+} ions stretch along axis $c(z)$. Mn^{3+} ions have a noncentral local environment in the form of pentagonal pyramids in layers with $z = 0.5c$. These pyramids are positioned in planes xy and couple octahedra chains with Mn^{4+} ions. R^{3+} ions have an environment similar to that of Mn^{3+} and are positioned in layers with $z = 0$ [3]. The structure of RMn_2O_5 is presented in Fig. 1.

Charge ordering and a finite probability of transfer of e_g electrons between $Mn^{3+}-Mn^{4+}$ ion pairs (double exchange [4,5]) are the crucial factors that define the multiferroic properties of RMn_2O_5 at all temperatures.

The low-temperature ferroelectric state at $T \leq T_C$ is due primarily to charge ordering along axis b. The alternation of pairs of neighboring Mn^{3+} and Mn^{4+} ions along axis b with a strong ferromagnetic (double) exchange and a weak indirect antiferromagnetic exchange leads to exchange striction, which distorts the centrosymmetricity of the lattice along axis b, and induces low-temperature ferroelectric ordering [6]. At the same time, the transfer of e_g electrons between $Mn^{3+}-Mn^{4+}$ ion pairs positioned in neighboring layers perpendicular to axis c produces phase separation nanoregions with the distribution of Mn^{3+} and Mn^{4+} ions differing from the one in the initial crystal matrix. These local regions in as-grown samples are both magnetic and ferroelectric. They exist in a temperature range spanning

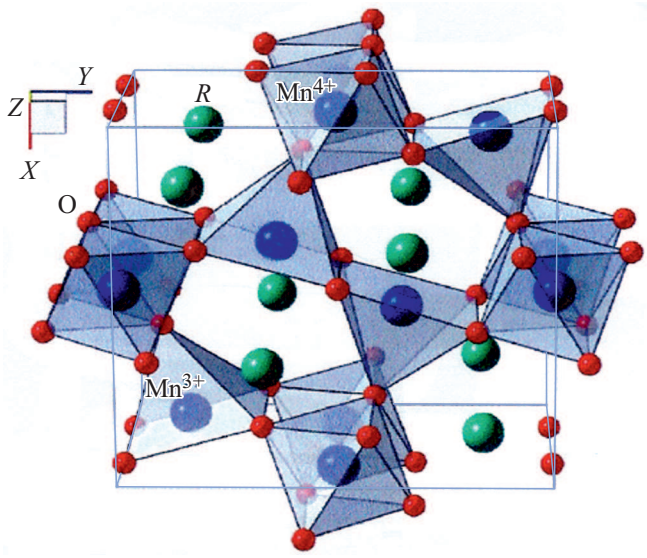

Figure 1. Structure of RMn_2O_5. Small red spheres represent oxygen ions; larger blue spheres, Mn^{4+} (in octahedra) and Mn^{3+} (in pentagonal pyramids) ions. The directions of crystal axes are indicated.

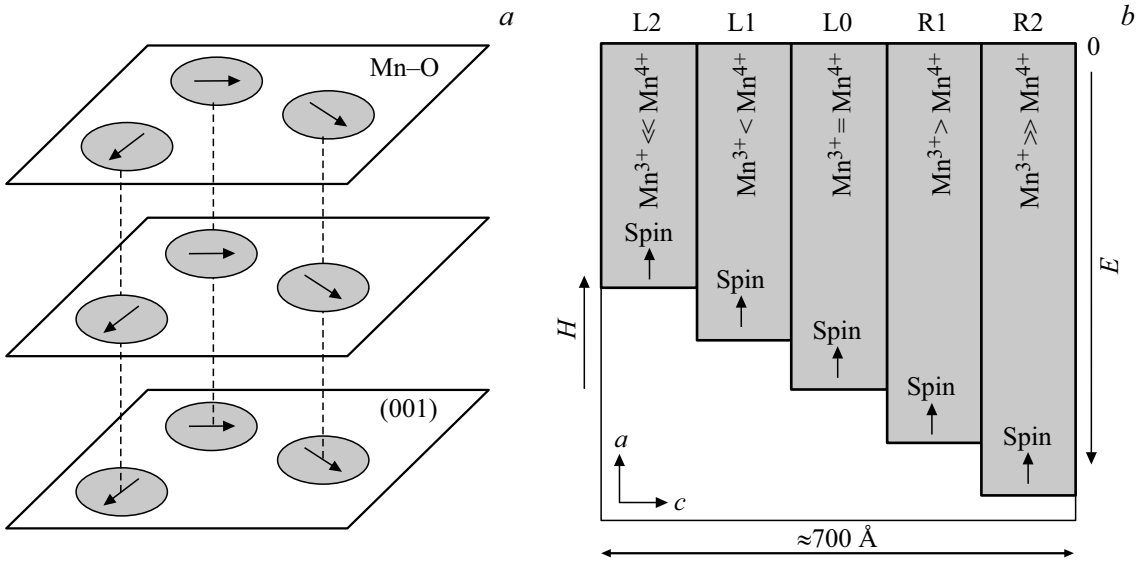

Figure 2. Schematic diagram of ferromagnetic 1D superlattices (shaded regions) in the initial crystal matrix (blank field); field $H = 0$ (a). Schematic diagram of one such superlattice in ECMO containing L_N ferromagnetic layers perpendicular to axis c with different densities of $Mn^{3+}-Mn^{4+}$ ion pairs and e_g electrons located in wells of a varying depth (shaded regions with different energies E) (b).

from low temperatures to those exceeding considerably the multiferroic ordering temperature. A strong magnetoelectric interaction in phase separation regions may persist up to high temperatures.

The states of phase separation regions were studied in RMn_2O_5 multiferroics and in doped $R_{0.8}Ce_{0.2}Mn_2O_5$ ($R =$ Eu, Gd, Tb, Bi) [7–21]. These papers were focused on the dielectric and magnetic properties, heat capacity, X-ray diffraction, Raman scattering [7–13], electric polarization [14–19], and μSR studies [20,21]. Note that the matrices of RMn_2O_5 crystals and doped $R_{0.8}Ce_{0.2}Mn_2O_5$ crystals had the same central symmetry $Pbam$.

Phase separation regions form in RMn_2O_5 and $R_{0.8}Ce_{0.2}Mn_2O_5$ in much the same manner as in $LaAMnO_3$ ($A =$ Sr, Ca, Ba) manganites, which also contain Mn^{3+} and Mn^{4+} ions [22–24]. They form in the initial crystal matrix as a result of self-organization processes due to the finite probability of tunneling of e_g electrons between $Mn^{3+}-Mn^{4+}$ ion pairs in the neighboring planes perpendicular to axis c. Just as in $LaAMnO_3$ ($A =$ Sr, Ca, Ba), this occurs in the context of balance between strong interactions: double exchange (with a characteristic energy of 0.3 eV), Jahn–Teller interaction (0.7 eV), and Coulomb repulsion (1 eV). As a result, they exist in a wide temperature range spanning from low temperatures to those exceeding room temperature [8–19]. The first two interactions facilitate the accumulation of electrons and $Mn^{3+}-Mn^{4+}$ ion pairs in phase separation regions, while the Coulomb repulsion establishes equilibrium electron density and shape of these regions [22–24]. The layered structure with $Mn^{3+}-Mn^{4+}$ ions distributed in layers perpendicular to axis c in the primary matrix of RMn_2O_5 and $R_{0.8}Ce_{0.2}Mn_2O_5$ crystals is retained in phase separation regions. As a result, phase separation regions form semiconductor heterostructures containing different numbers of Mn^{3+} (donor) and Mn^{4+} (acceptor) ions in superlattice layers. These heterostructures may be rendered as alternating isotropic ferromagnetic layers with ferromagnetic boundaries that do not interfere with the transfer of e_g electrons between layers in the process of double exchange. The properties of such heterostructures have been examined in most detail in $EuMn_2O_5$ (EMO) and $Eu_{0.8}Ce_{0.2}Mn_2O_5$ (ECMO) [8–12].

Fig. 2 illustrates this by presenting a schematic diagram of formation of ferromagnetic semiconductor heterostructures (1D superlattices) (Fig. 2, a) and a diagram of one superlattice of this kind in ECMO (Fig. 2, b) [25]. A set of ferromagnetic resonances (FMRs) from individual layers of superlattices was observed. The specific features of these FMRs provided insight into the properties of the layers and the superlattice as a whole. The intensity of individual superlattice FMR lines and their position with respect to the magnetic field are defined by the difference in numbers of ferromagnetic Mn^{3+} and Mn^{4+} ion pairs in superlattice layers. 1D superlattices in EMO and ECMO persist up to $T < 60$ K and $T < 80$ K, respectively. The sizes of phase separation regions in them are ≈ 900 Å (EMO) and ≈ 700 Å (ECMO) [8]. The balance of strong interactions mentioned above provides for the formation of dynamic equilibrium states of phase separation regions with a certain distribution of Mn^{3+} and Mn^{4+} ions in individual superlattice layers.

The present study is focused on investigating the influence of Er^{3+} ions, the ground state of which differs qualitatively from the state of Eu^{3+} ion in ECMO, on the properties of 1D superlattices of phase separation regions in $ErMn_2O_5$ (ErMO). Eu^{3+} ions in ground state $^7F_0$ are

almost nonmagnetic. These are the so-called Van Vleck ions characterized by a weak admixture of the first excited magnetic state $^7F_1$, which is shifted by $\approx 300\,\mathrm{cm}^{-1}$ from the ground state and has almost no effect on the properties of ECMO. The ground state of Er^{3+} ($^4I_{15/2}$, $S = 3/2$, $L = 6$) ion has a strong magnetic moment ($J = 9.6\,\mu_B$), the key contribution to which is provided by the orbital moment, and a strong crystal field emerges and makes the orientation of moments Er ions fixed rigidly along axis c, thus inducing strong single-ion anisotropy. Compared to ECMO, ErMO thus features additional interactions that form a different distribution of $Mn^{3+}-Mn^{4+}$ ion pairs in superlattice layers. Charge ordering is retained in this case (the equality of $Mn^{3+}-Mn^{4+}$ ion densities in the entire superlattice is dictated by the strong electrostatic interaction and charge conservation). Thus, ErMO and ECMO differ both in the magnitude of the exchange magnetic interaction of R ions with the subsystem of manganese ions and in the anisotropy of this interaction. The spins of $Mn^{3+}-Mn^{4+}$ ion pairs in ErMO are oriented rigidly along axis c, while the same spins in ECMO are reoriented relatively easily by an applied external magnetic field and align with it [10,11].

A comparative examination of the magnetic properties, the heat capacity, the magnetic dynamics (set of ferromagnetic resonances from superlattice layers), and the electric polarization of ErMO was carried out in the present study. Special attention was paid to the features of phase separation regions in ErMnO. The characteristic features of ErMO attributable to the influence of Er^{3+} ions and consistent over different measurements were revealed.

2. Research methods and objects under study

ErMO single crystals were grown by spontaneous crystallization from solution-melt [26,27]. They had the form of plates with a thickness of $2-3$ mm and an area of $3-5\,\mathrm{mm}^2$. The symmetry of crystals and their composition were determined by X-ray phase analysis and X-ray fluorescence spectroscopy, respectively. All crystals were plate-like faceted with well-defined axes. Axis c was usually perpendicular to the extended surface of plates, and the orientations of axes a and b were defined unambiguously. ErMO single crystals with natural faceting were used for measurements.

The dynamic magnetic susceptibility of ErMO was measured using the induction method at 10 kHz. A sample with a chosen orientation was introduced into one of the two measuring coils, which were compensated prior to the experiment, and the decompensation signal induced by the magnetic moment of the sample was measured. A transmission-type magnetic resonance spectrometer with low-amplitude magnetic modulation was used to perform FMR measurements. These measurements were carried out in the $5-300$ K temperature range at frequencies ranging from 30 to 40 GHz in a magnetic field up to 2 T generated by an electromagnet. A cryostat with optical windows was introduced into the microwave channel that ensured uniformity of the microwave field distribution in the vicinity of the sample. Static magnetic field H was perpendicular to the direction of the microwave field propagation (wave vector k). The detected FMR signals were amplified by a lock-in SR530 amplifier.

A Quantum Design physical property measurement system was used to determine the heat capacity.

Flat capacitors with a thickness of $0.3-0.6$ mm and an area of $3-4\,\mathrm{mm}^2$ were fabricated to measure the dielectric properties and the polarization. The permittivity and the conductivity were measured using a Good Will LCR-819 impedance meter in the $0.5-50$ kHz frequency range.

The electric polarization was measured in accordance with the PUND (positive-up-negative-down) technique. We used the PUND method adapted to measurements of the polarization of local polar regions with local conductivity [15,16,18].

3. Experimental data and analysis

3.1. Magnetic dynamics (set of ferromagnetic resonances from layers of superlattices of phase separation regions) in ErMO.

As was demonstrated in the study of FMRs in ECMO [9,10], the distribution of intensities of FMR lines from individual layers of phase separation regions provides insight into the properties of layers and the superlattice as a whole. It is convenient to study the features of magnetic dynamics in ErMO by comparing these dynamics in ErMO and ECMO. As was already noted, Eu^{3+} ions in the ground state are almost nonmagnetic and weakly coupled to the lattice. On the contrary, Er^{3+} ions are highly magnetic and heavily distort the lattice. Fig. 3, *a* and *b* present the sets of FMR lines from superlattice layers in ECMO and ErMO, respectively.

The dynamic equilibrium state of superlattice layers in ECMO shown in Fig. 3, *a* was established after three consecutive magnetic field increase/decrease cycles in FMR measurements.

The states of superlattice layers changed gradually in the process of field cycling, and the states after each cycle were sufficiently long-lived for successive changes to accumulate from one cycle to the other. The magnetic field increase/decrease time (the length of one half of the cycle) was ~ 15 min at a rate of 1.2 kOe/min. The intensities of FMR signals from individual superlattice layers are proportional to their magnetization (i.e., the number of ferromagnetic pairs of Mn^{3+} and Mn^{4+} ions in these layers). In a dynamic equilibrium state, the most intense FMR line is the one from layer L0, which features equal numbers of Mn^{3+} and Mn^{4+} ions. A dielectric state with charge ordering is established in this layer. The number of Mn^{4+} ions in left layers L2, L1 exceeds the number of Mn^{3+} ions. These layers feature hole conductivity, and the intensities of

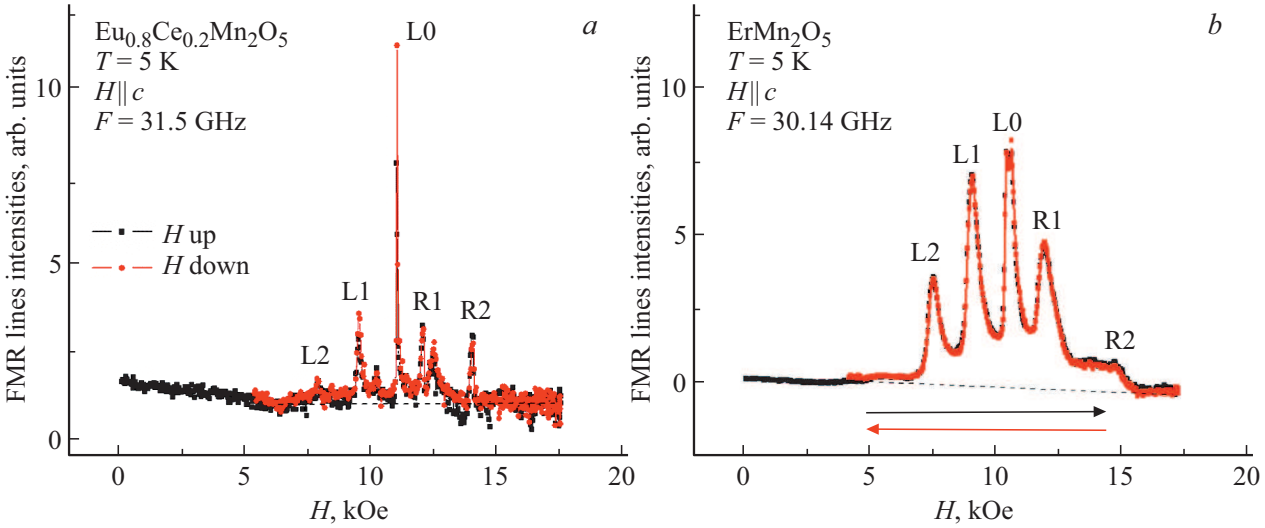

Figure 3. Sets of FMR lines from superlattice layers in ECMO (a) ($F = 31.5$ GHz) and ErMO (b) ($F = 30.14$ GHz). $H \parallel c$. $T = 5$ K.

their FMR lines are considerably lower than the intensities corresponding to layer L0. The number of Mn^{3+} ions in right layers R2, R1 exceeds the number of Mn^{4+} ions. These layers feature electron conductivity, and the intensities of their FMR lines are also considerably lower than the intensities corresponding to layer L0. A semiconductor heterostructure with charge compensation of left and right layers with respect to layer L0 is thus formed. Note also that all lines in ECMO have a zero absorption background, which is indicated with dashes in Fig. 3, *a*. The schematic distribution of energy wells for the superlattice layers in ECMO is shown in Fig. 2, *b*. The distribution of intensities of FMR signals in ErMO is qualitatively different (Fig. 3, *b*). The same five FMR lines are seen in ErMO, but they are substantially broader and have a significantly different ratio of intensities. The lines are unresolved at the bases and thus form a nonzero background. Importantly, a complete set of FMR lines in ErMO forms, in contrast to ECMO, in the very first cycle of variation of the magnetic field oriented along axis *c*. If the field is oriented along axes *a* and *b*, FMR lines are not observed at all.

The set of FMR lines in ErMO obtained in the first variation cycle of the field applied along axis *c* does not change in subsequent cycles. This suggests that ErMO features an internal field with its strength sufficient to establish the initial ground state of superlattices, which is recorded in the very first measurement of FMR signals. Thus, the ground dynamic equilibrium state of superlattices in ErMO is self-induced by internal interactions. In contrast, the dynamic equilibrium (long-lived) state in ECMO is established by cycling the magnetic field. The internal interaction causing the above effect is the interaction of Er^{3+} ions with Mn^{3+} and Mn^{4+} ions. It is worth reminding that Er^{3+} ions have a strong magnetic moment. A significant contribution to it is produced by the orbital moment, which distorts the lattice heavily along axis *c*. The chains

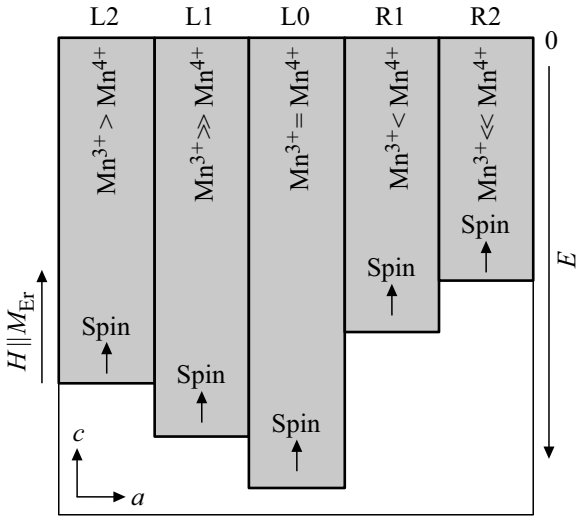

Figure 4. Schematic distribution of depths of wells of superlattice layers in phase separation regions in ErMO.

of octahedra with Mn^{4+} ions in $ErMn_2O_5$ extend along the same axis (Fig. 1). Therefore, Er^{3+} ions distort the octahedra with Mn^{4+} ions most heavily along axis *c*, deepening the wells for layers L1 and L2. As a result, electrons from the layers to the right (L0, R1, R2) migrate into these layers, thus increasing the number of Mn^{3+} ions and the number of ferromagnetic Mn^{3+}–Mn^{4+} ion pairs in superlattice layers L1 and L2 and establishing a new dynamic equilibrium state in the entire superlattice.

Having analyzed the experimentally observed ratio of intensities of FMR lines in ErMO, we may plot schematically the distribution of depths of wells of superlattice layers and the relation between the numbers of Mn^{3+} and Mn^{4+} ions in individual layers (see Fig. 4). Layer L0 with charge ordering is still the most stable and energetically favorable.

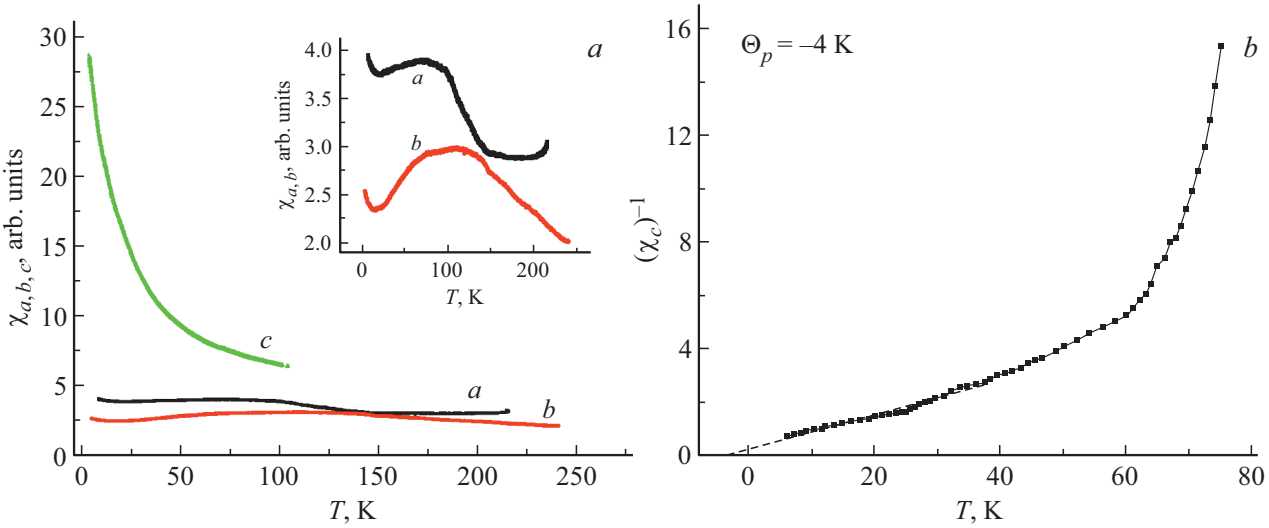

Figure 5. Temperature dependences of the dynamic magnetic susceptibility of ErMO along different axes (indicated next to the curves). The susceptibilities along axes a and b are shown on a smaller scale in the inset (a). Temperature dependence of the inverse magnetic susceptibility of ErMO along axis c (b).

The numbers of Mn^{3+} and Mn^{4+} ions in it are equal; a dielectric state with the maximum number of ferromagnetic Mn^{3+}–Mn^{4+} ion pairs emerges. This corresponds to the most intense and the narrowest FMR line (Fig. 3, *b*). The L0 well is the deepest (Fig. 4). As was already noted, the well depths and the FMR line intensities of layers L1, L2 in ErMO exceed the corresponding values for R1, R2 and are fairly close to the values characterizing layer L0 (Fig. 4). Electrons from shallower layers migrate into deeper layers L1, L2, thus increasing the number of Jahn–Teller Mn^{3+} ions in octahedra via the $Mn^{4+} + e = Mn^{3+}$ reaction. This also enhances the well depth of these layers. As a result, Mn^{3+} ions are predominant in deep layers L1, L2 in ErMO, while Mn^{4+} ions are predominant in layers R1, R2 (Fig. 4). In other words, the properties of layers L1, L2 and R1, R2 in ErMO are inverted with respect to those in ECMO (cf. Fig. 4 and Fig. 2, *b*).

ErMO differs qualitatively from ECMO in one other respect. In the equilibrium state of ECMO, the symmetric distribution of charges in left and right layers relative to the L0 line set against the zero background of the crystal matrix resulted in charge compensation of these left and right superlattice layers and in the lack of spontaneous electric polarization in zero external electric field. As will be shown below, the violation of symmetry of the ratio of intensities for lines L1, L2 and R1, R2 relative to line L0 and the distortion of the ErMO matrix background of these lines is indicative of the violation of charge compensation and the emergence of electric polarization in ErMO.

3.2. Magnetic properties of $ErMn_2O_5$. The effect of phase separation regions on them.

Fig. 5, *a* presents the dynamic magnetic susceptibilities along different axes of the ErMO crystal. These susceptibilities are proportional to the magnetic moments of samples in the corresponding directions. Since all crystals of the RMn_2O_5 multiferroic family with different rare-earth ions (nonmagnetic Y and Bi ions included) have close Néel temperatures $T_N \sim 40$ K, it is fair to say that magnetic ordering in all these multiferroics is governed by the subsystem of manganese ions. The magnetic ordering of R^{3+} ions in compounds with 3*d* ions (orthoferrites and orthochromites) usually occurs at low temperatures (5–10 K).

The magnetic susceptibility along axis *c* increases sharply in ErMO as the temperature decreases down to 5 K (Fig. 5, *a*). This increase is associated with Er^{3+} ions. At the same time, the susceptibility maximum, which is typical of their magnetic ordering, is not observed. Therefore, Er^{3+} ions remain in the paramagnetic state within the entire examined temperature range (from 5 K upwards). Note also that no anomalies of the susceptibility along axis *c* are observed in the vicinity of 44 K, which is the temperature of magnetic ordering of the Mn subsystem of the crystal matrix. This suggests that the susceptibility along axis *c* is governed primarily by Er^{3+} ions.

The paramagnetic susceptibility of Er^{3+} ions along axis *c* at $T > 5$ K follows the Curie–Weiss law: $\chi = C_M/(T - \theta_p)$, where χ is the magnetic susceptibility; C_M is the Curie constant, which allows one to determine the effective magnetic moment; θ_p is the Curie temperature below which spontaneous magnetization emerges (Fig. 5, *b*). It can be seen that the temperature dependence of the inverse susceptibility is linear in the 5–65 K range, although the slope of $\chi^{-1}(T)$ changes slightly at $T \approx 25$ K. The values of the Curie temperature and the effective magnetic moment derived from the Curie–Weiss law are $\theta_p = -4$ K and $\mu \sim 7\,\mu$B, respectively. The determined effective magnetic

moment of Er^{3+} ions turned out to be lower than the moment of an isolated Er^{3+} ion ($9.6\mu B$).

Thus, the magnetic ordering of Er ions in ErMO may occur only at $T < T_{N1} \approx 4$ K. At temperatures $T > T_{N1}$, Er ions are paramagnetic and oriented along axis c by the internal effective field, which is associated with the orbital contribution to the Er moment, and the effective field of the Er–Mn exchange interaction. At the same time, the paramagnetic susceptibility of Er ions along axis c at $T > T_{N1}$ is significantly higher than the magnetic susceptibilities of ErMO crystals along axes a and b (Fig. 5, a). As was already noted, the orientation of Er magnetic moments is also affected by the effective internal Er–Mn exchange field, which depends on spin orientations and the values of magnetic moments of Mn ions. It was noted above that the magnetic susceptibilities of ErMO in plane ab (Fig. 5, a and its inset) are governed primarily by manganese ions positioned in layers ab (Fig. 1). Ferromagnetic Mn^{3+}–Mn^{4+} ion pairs in phase separation regions have the highest magnetic susceptibilities. However, Fig. 5, a demonstrates that these susceptibilities are lower than the contribution to the measured susceptibility along axis c, which is apparently attributable to the fact that the density of phase separation regions in the bulk of an ErMO crystal is low (just as in EMO and ECMO [7–10]).

The magnetic susceptibilities along axes a and b are shown on an enlarged scale in the inset of Fig. 5, a. It can be seen that the susceptibilities increase as the temperature decreases in the 5–25 K interval. In the 25–65 K range, the susceptibilities increase with temperature. Thus, the temperature variation of the susceptibility of the manganese subsystem changes its sign in the vicinity of 25 K (inset of Fig. 5, a). The temperature dependences of $\chi(T)$ along axes a and b reach plateaus in the vicinity of $T \approx 65$ K and then descend slowly within the ~ 150–170 K range (along axis a) and near 250 K (along axis b) (inset of Fig. 5, a). Thus, the anomalous behavior of the inverse susceptibility of ErMO near 25 K and a fairly significant change in the slope of its temperature dependence near 65 K (Fig. 5, b) are indicative of a change in the state of Mn ions in the vicinity of these temperatures.

The effective magnetic field of Er^{3+} ions along axis c is transverse with respect to the phase separation regions containing ferromagnetic Mn^{3+}–Mn^{4+} ion pairs and electrons involved in the double exchange between these ions in layers ab. It induces precession of electrons within the phase separation regions and gives rise to the diamagnetic response that reduces the effective moment of Er ions along axis c. This is the reason why the effective magnetic moment of Er^{3+} ions derived from the Curie–Weiss law for ErMO is lower than the corresponding value for an isolated Er^{3+} ion (see above). It turned out that the phase separation regions of the Mn subsystem also contribute to the reduction of the moment of Er ions in ErMO. Thus, the self-consistent interplay between magnetic Er and Mn subsystems due to the Er–Mn exchange interaction is characterized by the temperature correlations in variations of the states of Er–Mn subsystems. A sharp increase in the magnetization of Er ions with decreasing temperature amplifies the diamagnetic response of electrons in phase separation regions. This response, in turn, depends on the density of electrons involved in the charge exchange of ferromagnetic Mn^{3+}–Mn^{4+} ion pairs in these regions and governs their magnetic moment. The density of these electrons decreases when the field of Er ions grows stronger as the temperature drops to 25 K. At $T < 25$ K, the diamagnetic response does not grow stronger, and the moments of manganese ions increase with decreasing temperature in accordance with the Curie–Weiss law. The specified process governs the behavior of the susceptibility of the manganese subsystem below 65 K (inset of Fig. 5, a).

The magnetic contribution of phase separation regions of Mn ions along axes a and b at $T > 65$ K is the most pronounced when the susceptibilities along these axes reach temperature plateaus with a slower reduction at temperatures rising to the levels indicated above (inset of Fig. 5, a). It is natural to associate these limit temperatures at which the high-temperature magnetic susceptibilities drop with temperatures at which thermal energy kT becomes equal to the height of barriers at the boundaries of phase separation regions, inducing a dramatic change in the states of phase separation regions. A frozen superparamagnetic state characterized by the presence of magnetic hysteresis loops exists below these temperatures [28]. At higher temperatures, phase separation regions are in the normal superparamagnetic state with no remanent magnetizations in zero magnetic field.

3.3. Dielectric and polar properties of ErMO and manifestations of the properties of phase separation regions in them.

We have examined the ferroelectric state of ErMO in [18]. The temperature dependence of permittivity along axis b in a wide range of temperatures, which is needed to determine the temperature interval of existence of an ordered ferroelectric state in ErMO, is presented in Fig. 6, a. The inset of Fig. 6, a shows the frequency-independent maxima of permittivity ε' in the vicinity of Curie temperature $T_C \approx 39$ K, which suggest that a ferroelectric phase transition occurs at this temperature.

At $T > T_C$, hysteresis loops with remanent polarization along all axes in ErMO were observed in [18] up to temperatures significantly higher than T_C. This was attributed to the presence of high-temperature polar phase separation regions that form a frozen superparaelectric state exhibiting hysteresis loops of electric polarization. It can be seen from Fig. 6, a that the frequency-independent permittivity ε' along axis b is the lowest and remains temperature-independent up to ~ 270 K. If the temperature increases further, the frequency-dependent rise of ε' is observed. Fig. 6, b presents the hysteresis loops of electric polarization along axis b. It is evident that hysteresis loops exist at temperatures ranging from the lowest ones to the temperature close to

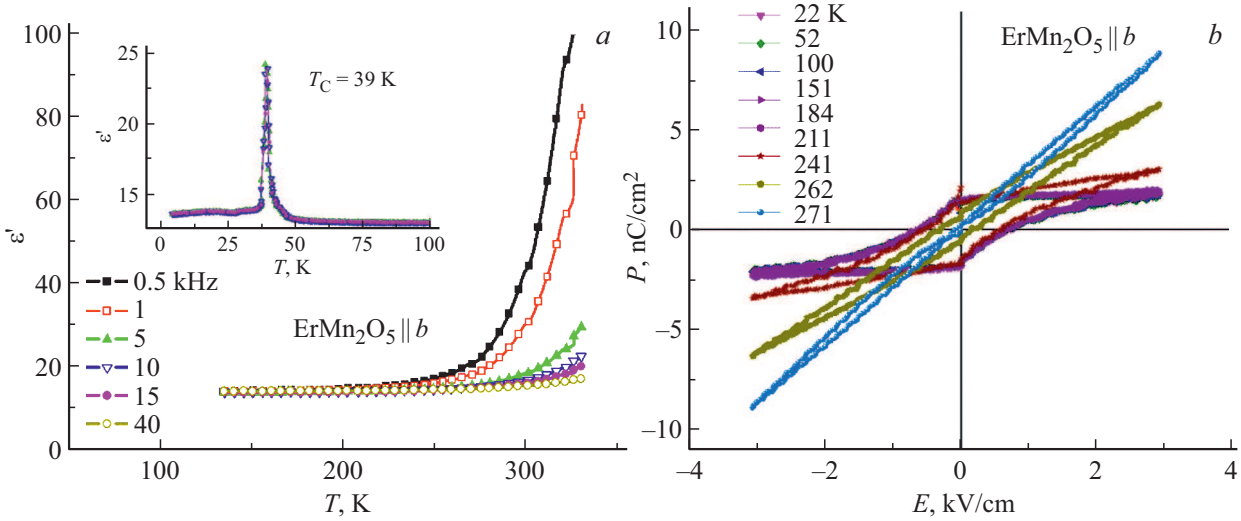

Figure 6. Temperature dependences of ε' along axis b for a number of indicated frequencies. The maxima of ε' for axis b, which have no frequency dispersion, are shown in the inset. Loops of electric polarization of ErMO along axis b measured using the PUND technique at a number of different temperatures (b) [18].

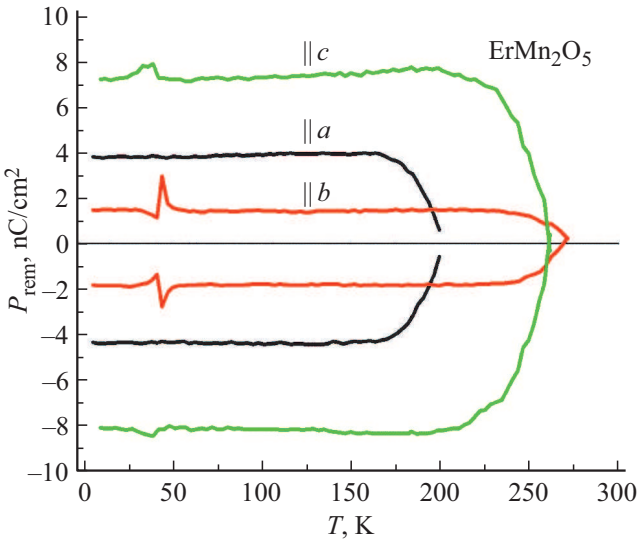

Figure 7. Temperature dependences of remanent polarization P_{rem} in electric polarization loops measured along all axes of the crystal [18].

that at which the frequency-dependent permittivity starts increasing rapidly (Fig. 6, a). The same remains true for the permittivity and the electric polarization along axes a and c up to a temperature of ~ 170 K and ~ 250 K, respectively.

Fig. 7 presents the temperature dependences of remanent polarization P_{rem} of electric polarization loops for all axes of ErMO. These dependences reveal the magnitudes of electric polarization for the corresponding axes and the maximum temperatures at which such polarizations exist. The low-temperature anomalies in the dependences of P_{rem} along axis b at ~ 39 K correspond to the low-temperature ferroelectric transition of the ErMO crystal matrix (see the inset of Fig. 6, a). The broad low-temperature anomaly of P_{rem} along axis c below ~ 40 K is indicative of a structural change in phase separation regions induced by Er^{3+} ions.

The polarity of phase separation regions in all the studied RMn_2O_5 crystals stems from the following two factors. As a result of the double exchange within these regions, which is associated with the transfer of e_g electrons between Mn^{3+}–Mn^{4+} ion pairs, Jahn–Teller Mn^{3+} ions occupy the positions of Mn^{4+} ions (oxygen octahedra) and distort these octahedra. At the same time, smaller (compared to Mn^{3+}) Mn^{4+} ions end up in noncentral pentagonal pyramids and also distort them additionally. Both factors contribute to the noncentrosymmetricity of phase separation regions and to their polarity [15–18]. These regions establish a superparaelectric state. Below certain temperatures, it is in a frozen superparaelectric state. The response of local polar regions in such a state to an applied electric field has the form of hysteresis loops of electric polarization with remanent polarization.

The frozen superparaelectric state for local ferroelectric regions in a dielectric centrosymmetric matrix has already been examined theoretically [29] and observed experimentally in RMn_2O_5 (R = Gd, Bi, Tb, Er) [15,16,18,19]. It was demonstrated in these studies that the frozen superparaelectric state persists up to those temperatures at which the kinetic energy of free charge carriers becomes equal to the height of barriers on the boundaries of regions. As the results presented above suggest, the same criterion applies to the temperatures of existence of the magnetic compare (cf. the inset of Fig. 5, a for axes a and b and Fig. 7). Thus, phase separation nanoregions are indeed multiferroic and persist up to temperatures that exceed considerably the temperatures of magnetic and ferroelectric ordering of the crystal matrix.

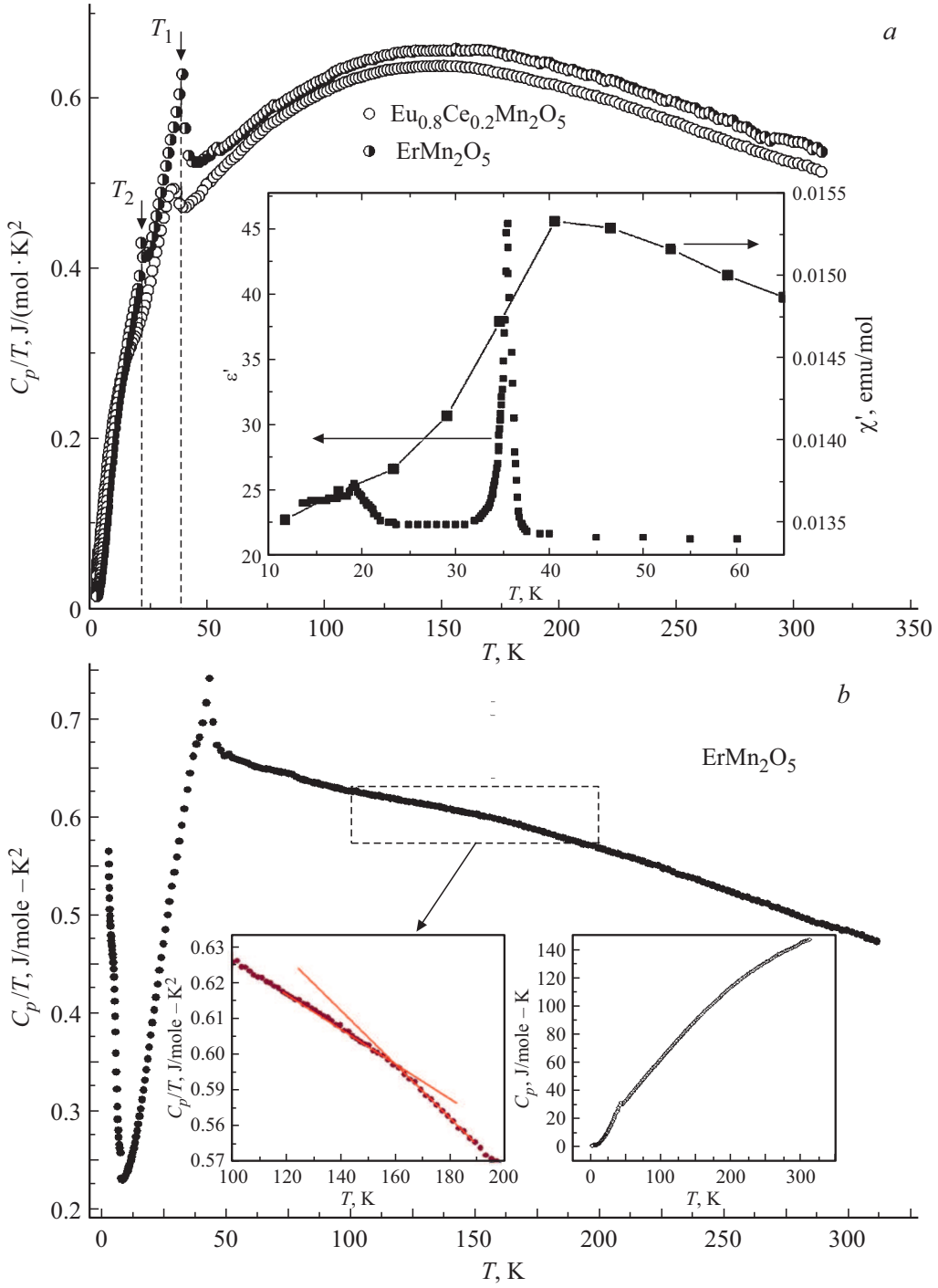

Figure 8. (a) Temperature dependence of C_p/T for ECMO and $EuMn_2O_5$. Temperatures of the magnetic and ferroelectric phase transitions in $EuMn_2O_5$, which are also relevant to the ECMO matrix [7], are demonstrated in the inset. (b) Temperature dependence of C_p/T for ErMO. The behavior of C_p/T in the 100–200 K interval is shown on a smaller scale in the left inset. The right inset presents the temperature dependence of heat capacity C_p in the entire temperature interval.

3.4. Temperature dependence of the heat capacity of ErMO.

It follows from the results of magnetic and dielectric studies that two types of phase transformations occur in ErMO crystals: phase transformations in 2D phase separation regions and magnetic and ferroelectric phase transitions in the crystal matrix. These transformations are observed up to the limit temperatures of existence of frozen superparamagnetic and superparaelectric states. Let us examine how these state changes manifest themselves in the temperature dependence of the heat capacity of

ErMO. ln doing that, we will compare the obtained data with the heat capacities of ECMO and EMO investigated in [7]. Fig. 8, *a* presents the temperature dependences of the heat capacity of ECMO and EMO [7]. As was already noted, Van Vleck Eu^{3+} ions in ECMO with ground state $^7F_0$ are weakly magnetic, and their magnetic moment increases with temperature merely due to the admixture of excited magnetic state $^7F_1$. The magnetic moment of Eu^{3+} ions is small and oriented in plane *ab* at all temperatures. The magnetization of the manganese subsystem in ECMO and EMO is also oriented in plane *ab*, and a transverse field inducing the diamagnetic response in the manganese subsystem is lacking. Thus, the effective field induced by the magnetization of Eu^{3+} ions has little effect on the states of manganese subsystems of these compounds. In EMO, well-pronounced anomalies of the heat capacity are observed in the vicinity of temperatures $T_1 = 39$ K, $T_2 = 21$ K. They are associated with the antiferromagnetic and ferroelectric phase transitions, respectively. These transitions were observed in [30].

The temperature dependences of C_p/T for ECMO reveal anomalies that are shifted toward lower (relative to EMO) temperatures: one anomaly in the vicinity of 34 K and another diffuse anomaly near 15 K (Fig. 8, *a*). They are also associated with the sequence of antiferromagnetic and ferroelectric phase transitions. Thus, the behavior of the heat capacity in ECMO and EMO at low temperatures ($T < 50$ K) is governed by the dynamics of both phonon and magnetic subsystems [7]. The dependence of $C_p/T(T)$ in ErMO crystals is fundamentally different (Fig. 8, *b*). In the high-temperature region (at $T > 60$ K), C_p/T varies linearly with a break in the vicinity of 160 K (left inset of Fig. 8, *b*). The temperature dependence of heat capacity C_p/T in ECMO and EMO is, in contrast, significantly nonlinear at high temperatures (Fig. 8, *a*). The above-mentioned change in the linear slope of the temperature dependence of the heat capacity in ErMO correlates with the temperature at which frozen superparamagnetic and superparaelectric states of phase separation regions along axis *a* vanish (left inset of Fig. 8, *b* and Fig. 7). In the low-temperature region, the temperature dependences of C_p/T in ErMO feature two anomalies: a narrow one with its maximum at $T_1 = 43$ K and a broad anomaly in the form of a break in the vicinity of 39 K against the backdrop of a sharp C_p/T decrease with decreasing temperature. The indicated temperatures of $C_p/T(T)$ anomalies are close to the temperatures of magnetic ordering ($T_N = 44$ K) and the ferroelectric phase transition ($T_C = 39$ K) in ErMO.

It is natural to attribute the substantial difference in behavior of the heat capacities of ErMO (Fig. 8, *b*) and ECMO (Fig. 8, *a*) to the influence of a strongly magnetic Er^{3+} ion with a large orbital contribution on the manganese subsystem, since no such influence is present in ECMO.

The difference between the influences of Er^{3+} and Eu^{3+} ions in ErMO (Fig. 8, *b*) and ECMO (Fig. 8, *a*), respectively, on the low-temperature heat capacity is especially significant. This is attributable to the fact that both crystals feature phase transitions from commensurate magnetic phases to incommensurate ones at temperatures below those of magnetic and ferroelectric ordering, and the wave vectors of magnetic structures change abruptly in these transitions. Ferroelectric ordering is normally established in the interval of existence of commensurate magnetic phases and is affected only slightly by low-temperature magnetic commensurate-incommensurate phase transitions [2]. ErMO differs from the other RMn_2O_5 multiferroics in that anomalous low-temperature incommensurate magnetic phase LT 1DICM emerges in it below $T \sim 8$ K. The electric polarization drops abruptly in this phase. As was already noted, ferroelectric polarization of an exchange-striction nature in RMn_2O_5 is established along axis *b* due to the exchange striction in the commensurate magnetic phase. The coupling of Er^{3+} ions with the lattice along crystal axis *c* becomes much stronger, thus enhancing the field of coercive polarization, which is caused by the exchange striction, and inducing an abrupt polarization reduction [2]. We associate the sharp C_p/T increase at temperatures below $T < 8$ K (Fig. 8, *b*) with the phase transition to phase LT 1DICM.

4. Conclusion

A comprehensive analysis of the magnetic and ferroelectric properties, the heat capacity, and the microwave magnetic dynamics of $ErMn_2O_5$ was carried out. Ferroelectric ordering of the crystal matrix in this multiferroic material is induced by its magnetic ordering. These orderings are established at low and close (39 and 44 K, respectively) temperatures and provide for a strong magnetoelectric coupling. The presence of charge ordering, which stems from the fact that equal numbers of Mn^{3+} and Mn^{4+} ions are positioned in neighboring players perpendicular to crystal axis *c*, is the specific feature of $ErMn_2O_5$. Owing to the finite probability of tunneling of e_g electrons between neighboring $Mn^{3+}-Mn^{4+}$ ion pairs, the spontaneous formation of phase separation nanoregions is energetically favorable. These regions are semiconductor heterostructures containing alternating ferromagnetic layers with different magnetic moments that depend on the number of ferromagnetic $Mn^{3+}-Mn^{4+}$ ion pairs in individual layers of superlattices (heterostructures). Phase separation regions forming due to self-organization occupy a small volume in the crystal matrix. The ground dynamic equilibrium state of phase separation regions is established in the context of balance between strong interactions: double exchange (with a characteristic energy of 0.3 eV), Jahn–Teller interaction (0.7 eV), and Coulomb repulsion (1 eV). This is the reason why they exist in a wide temperature range (from low temperatures to those exceeding room temperature), being multiferroic with a strong magnetoelectric interaction. The influence of Er^{3+} ions, which have a strong magnetic moment with a significant orbital contribution providing for a strong coupling with the lattice, was examined for the

first time. It was demonstrated that exactly this influence of Er^{3+} ions in $ErMn_2O_5$ gives rise to the spontaneous electric polarization of phase separation regions that coexists with their ferromagnetic ordering. The influence of Er^{3+} ions on the states of conductive ferromagnetic phase separation regions produces a complex pattern of temperature variations of the magnetization in ErMO that is governed by the self-consistent mutual influence of magnetic Er and Mn subsystems via the Er−Mn exchange interaction. It was found that the value of C_p/T in ErMO increases sharply at temperatures below 8 K. This increase is attributable to the low-temperature one-dimensional incommensurate magnetic phase transition to phase LT 1DICM that induces an abrupt reduction in the exchange-striction electric polarization. This stems from the specific features of the ground state of Er^{3+} ions.

Conflict of interest

The authors declare that they have no conflict of interest.

References

[1] N. Hur, S. Park, P.A. Sharma, J.S. Ahn, S. Guba, S.-W. Cheong. Nature (London) **429**, 392 (2004).
[2] Y. Noda, H. Kimura, M. Fukunaga, S. Kobayashi, I. Kagomiya, K. Kohn. J. Phys.: Condens. Matter **20**, 434206 (2008).
[3] P.G. Radaelli, L.C. Chapon. J. Phys.: Condens. Matter **20**, 434213 (2008).
[4] P.G. de Gennes. Phys. Rev. **118**, 141 (1960).
[5] L.P. Gor'kov, Phys.-Usp. **168**, 655 (1998).
[6] J. van den Brink, D.I. Khomskii. J. Phys.: Cond. Matter **20**, 434217 (2008).
[7] V.A. Sanina, E.I. Golovenchits, V.G. Zalesskii, S.G. Lushnikov, M.P. Scheglov, S.N. Gvasaliya, A. Savvinov, R.S. Katiyar, H. Kawaji, T. Atake. Phys. Rev. B **80**, 224401 (2009).
[8] V.A. Sanina, E.I. Golovenchits, V.G. Zalesskii, M.P. Scheglov. J. Phys.: Condens. Matter **23**, 456003 (2011).
[9] E.I. Golovenchits, V.A. Sanina, V.G. Zalesskii, JETP Lett. **95**, 429 (2012).
[10] V.A. Sanina, E.I. Golovenchits, V.G. Zalesskii. J. Phys.: Condens. Matter **24**, 346002 (2012).
[11] V.A. Sanina, B.Kh. Khannanov, E.I. Golovenchits, Phys. Solid State **59**, 1932 (2017).
[12] V.A. Sanina, E.I. Golovenchits, V.G. Zalesskii, B.Kh. Khannanov. J. Phys.: Condens. Matter **25**, 336001 (2013).
[13] B.Kh. Khannanov, V.A. Sanina, E.I. Golovenchits. J. Phys. Conf. Ser, **572**, 012046 (2014).
[14] V.A. Sanina, E.I. Golovenchits, B.Kh. Khannanov, M.P. Scheglov, V.G. Zalesskii. JETP Lett. **100**, 407 (2014).
[15] B.Kh. Khannanov, V.A. Sanina, E.I. Golovenchits, M.P. Scheglov. JETP Lett. **103**, 248 (2016).
[16] B.Kh. Khannanov, V.A. Sanina, E.I. Golovenchits, M.P. Scheglov. JMMM **421**, 326 (2017).
[17] V.A. Sanina, B.Kh. Khannanov, E.I. Golovenchits, M.P. Scheglov, Phys. Solid State **60**, 531 (2018).
[18] B.Kh. Khannanov, E.I. Golovenchits, V.A. Sanina, Phys. Solid State **62**, 257 (2020).
[19] B.Kh. Khannanov, E.I. Golovenchits, V.A. Sanina, Phys. Solid State **62**, 574 (2020).
[20] S.I. Vorob'ev, E.I. Golovenchits, V.P. Koptev, E.N. Komarov, S.A. Kotov, V.A. Sanina, G.V. Scherbakov, JETP Lett. **91**, 561 (2010).
[21] S.I. Vorob'ev, D.S. Andrievsky, S.G. Barsov, A.L. Getalov, E.I. Golovenchits, E.N. Komarov, S.A. Kotov, A.E. Moroslin, A.Yu. Mischenko, V.A. Sanina, G.V. Scherbakov, J. Exp. Theor. Phys. **150**, 1170 (2016).
[22] M.Yu. Kagan, K.I. Kugel', Phys.-Usp. **171**, 533 (2001).
[23] J. Lorenzana, J.C. Castellani, C. Castro Di. Europhys. Lett. **57**, 704 (2002).
[24] K.I. Kugel', A.L. Rakhmanov, A.O. Sboychakov, F.V. Kustmarsev, N. Poccia, A. Bianconi. Supercond. Sci. Technol. **22**, 014007 (2009).
[25] E.I. Golovenchits, B.Kh. Khannanov, V.A. Sanina, JETP Lett. **111**, 826 (1920).
[26] V.A. Sanina, L.M. Sapozhnikova, E.I. Golovenchits, N.V. Morozov, Fiz. Tverd. Tela **30**, 3015 (1988) (in Russian).
[27] A.V. Babinskii, E.I. Golovenchits, N.V. Morozov, L.M. Sapozhnikova, Fiz. Tverd. Tela **34**, 108 (1992) (in Russian).
[28] A. Maeda, T. Satake, T. Fujimori, H. Kuroda. J. Phys.: Condens. Matter **2**, 245 (1990).
[29] M.D. Glinchuk, E.A. Eliseev, A.N. Morozovska. Phys. Rev. B **78**, 134107 (2008).
[30] H. Nakamura, M. Ishikawa, K. Kohn, M. Ishikawa, J. Phys. IV France, C **1**, *7*, 365 (1997).